iScience

CellPress
OPEN ACCESS

Article

Expanding the solvent diversity and perovskite compatibility of SnO_2 inks that are directly deposited on perovskite layers

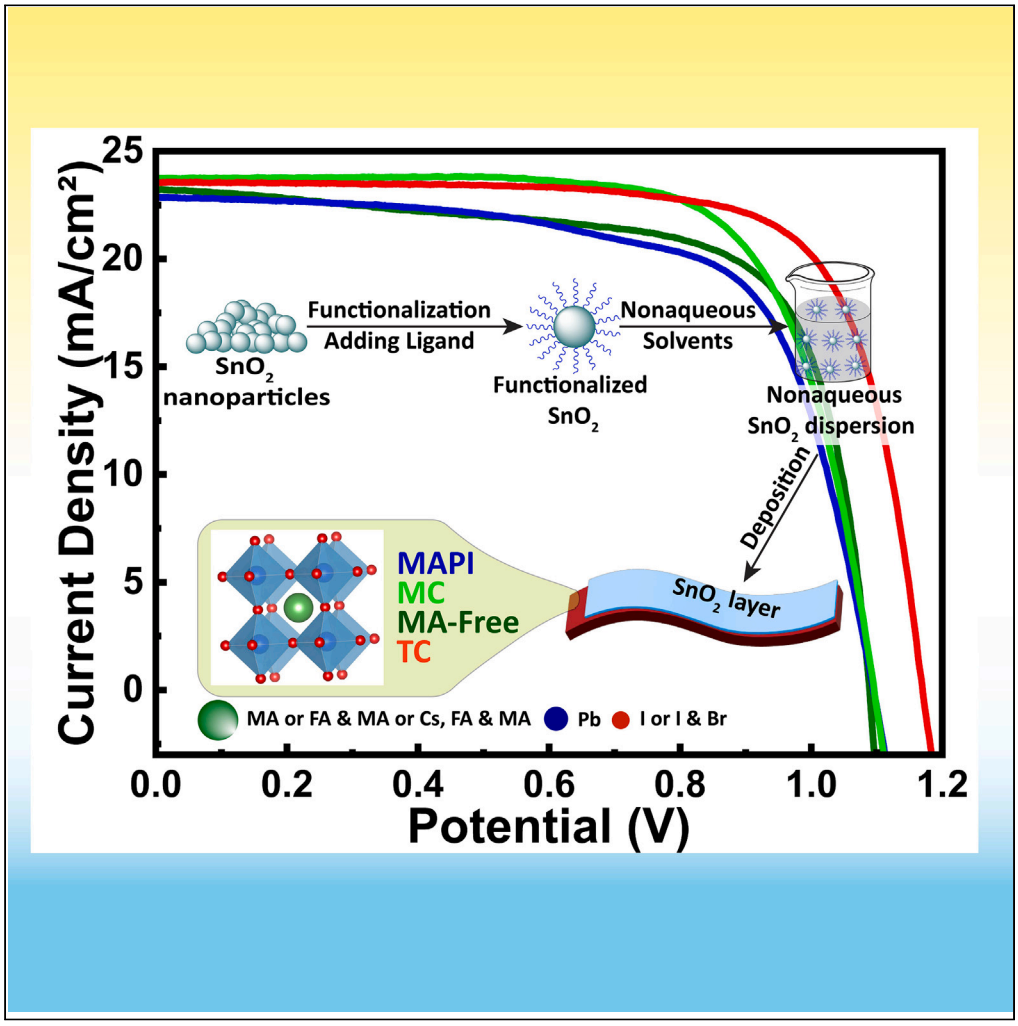

Sashil Chapagain, Peter J. Armstrong, Rojita Panta, Narayan Acharya, Thad Druffel, Craig A. Grapperhaus

thad.druffel@louisville.edu (T.D.)
craig.grapperhaus@louisville.edu (C.A.G.)

Highlights

Functionalized yttrium-doped tin(IV) oxide disperses in polar protic solvents

Dispersions are compatible with multiple perovskite formulations

Demonstrates SnO_2 as a cost-effective alternative in p-i-n perovskite solar cells

Champion device power conversion efficiency of 19.02% on flexible substrate

Chapagain et al., iScience 27, 110964
October 18, 2024
https://doi.org/10.1016/j.isci.2024.110964

iScience

CellPress
OPEN ACCESS

Article

Expanding the solvent diversity and perovskite compatibility of SnO_2 inks that are directly deposited on perovskite layers

Sashil Chapagain,[1] Peter J. Armstrong,[1] Rojita Panta,[1] Narayan Acharya,[1] Thad Druffel,[2,*] and Craig A. Grapperhaus[1,3,*]

SUMMARY

Tin oxide (SnO_2) is an attractive electron transport material (ETM) for perovskite solar cells (PSCs) due to its optoelectronic properties, low-temperature solution processability, cost, and stability. However, solvent incompatibilities have largely limited its application to devices with SnO_2 deposited below the perovskite. To expand its utility in other device structures, including inverted PSCs and tandem devices, alternate deposition strategies are needed. This study addresses the solvent scope and perovskite compatibility of acetate-stabilized yttrium-doped SnO_2 (Y:SnO_2) dispersions. We show that dispersions in several lower alcohols and select polar aprotic solvents can be directly deposited on perovskite using scalable and low-temperature processes. Further, they are compatible with various perovskite formulations, including those with mixed cations and mixed anions. The study expands the applicability of SnO_2 as a solution-processible and cost-effective ETM as an alternative to fullerene-based organic ETMs and serves as a guide for its use in PSCs and tandem devices.

INTRODUCTION

Halide perovskites hold promise for the next generation of thin-film photovoltaic materials owing to their low-cost solution processability and excellent optoelectronic properties. Over a decade of advancements in compositional engineering, defect passivation, interface engineering, and device fabrication techniques have driven the power conversion efficiency of halide perovskite solar cells (PSCs) from 3.8% to over 26%.[1–4] Simultaneously, their operational stability has improved remarkably, extending from a few seconds to several thousand hours.[1–3]

Inverted (p-i-n) architecture with fullerenes and their derivatives, such as C_{60}, C_{70}, $PC_{61}BM$, and $PC_{71}BM$, as a top layer electron transport layer (ETL) is becoming more common.[5,6] These ETLs exhibit superior electron mobility, low-temperature processability, and higher intrinsic stability as they do not require doping.[7] The use of undoped hole transport layers (HTLs) and intrinsically stable ETLs has been associated with improved stability and reduced hysteresis in inverted PSCs. Additionally, fullerenes and their derivatives are reported to passivate defects and suppress non-radiative recombination in perovskite films, thanks to their electron-rich heteroatoms or heterocycles.[8] Consequently, inverted PSCs with fullerenes as an ETL material have reached power conversion efficiencies exceeding 25% in single-junction planar structures on glass substrate and 23% on flexible substrate making inverted PSCs a promising option for practical applications.[9–11] Moreover, in perovskite/silicon tandem cells, using a p-i-n PSC with a thin ETL as the top cell substantially mitigates the loss of high-energy photons caused by parasitic absorption from the HTL in n-i-p PSCs as the top cell. This enhancement directly addresses a key limitation affecting short-circuit current density (a thin ETL for $_{SC}$) in perovskite/silicon tandem devices.[12] In the p-i-n architecture of PSCs, PCBM serves as a commonly used ETL material due to its solubility in nonpolar solvents and suitability for low-temperature processing.[13] However, PCBM exhibits poor morphological stability due to weak intermolecular interactions in the solid state. Consequently, PCBM coatings on perovskite films often aggregate, leading to an unfavorable surface morphology with voids and pinholes that facilitate perovskite degradation.[14,15] Additionally, the weak intermolecular interactions among fullerene molecules (such as C_{60} and PCBM) and the mismatched thermal expansion of fullerene-based ETLs with other layers in PSCs can result in delamination.[16] These challenges significantly impact the long-term stability of fullerene-based single-junction or tandem devices.

Despite their advantages, the broader adoption of fullerene-based ETLs in commercial applications faces significant challenges, particularly due to their high production costs and limited device stability.[7,17,18] Fullerene and its derivatives tend to self-aggregate, making these thin films prone to cracking and fracture, ultimately leading to device failure.[19–21] Additionally, their small molecular size and low solution viscosity might not provide complete surface coverage for optimized film thicknesses as an ETL.[19] Such incomplete coverage can lead to

[1]Department of Chemistry, University of Louisville, Louisville, KY 40292, USA
[2]Conn Center for Renewable Energy Research, University of Louisville, Louisville, KY 40292, USA
[3]Lead contact
*Correspondence: thad.druffel@louisville.edu (T.D.), craig.grapperhaus@louisville.edu (C.A.G.)
https://doi.org/10.1016/j.isci.2024.110964

direct contact between the electrode and the perovskite layer, accelerating device degradation.[5] Furthermore, fullerene derivatives are susceptible to reaction with air and moisture, which further contributes to the degradation process.[5]

To overcome these challenges, future research needs to prioritize the development of cost-effective alternatives to fullerenes, which will be vital in advancing the commercial viability of perovskite solar technology. Solution-processed tin oxide (SnO_2) has shown significant promise as an inexpensive and efficient ETL in the regular PSC architecture.[22,23] Furthermore, SnO_2 exhibits excellent electron mobility (approximately 200–250 $cm^2\ V^{-1}\ s^{-1}$) and demonstrates better band alignment with most state-of-the-art organic-inorganic halide perovskite compositions compared to TiO_2.[24–26] Its conduction band (CB) is well aligned with the CB of perovskites, while its valence band is deep enough to effectively block holes. This alignment results in smaller CB offsets when interfaced with perovskites, reducing the risk of significant overpotential and open-circuit voltage (V_{OC}) loss. Comparative analysis reveals that quasi-Fermi level splitting values at the SnO_2/perovskite interface in an n-i-p device structure surpass those at the TiO_2/perovskite and C_{60}/perovskite interfaces, as well as the perovskite/PCBM interface in the p-i-n architecture.[27] This indicates that a higher maximum V_{OC} can be achieved with SnO_2 ETL interfaced with perovskite, highlighting its superior performance. Pre-synthesized SnO_2 nanoparticles offer great tunability. Doping SnO_2 nanoparticles with metal cations like Li^+, Mg^{2+}, Y^{3+}, Zr^{4+}, Nb^{5+}, and W^{6+} during synthesis modulates electrical properties, including carrier concentration and electron mobility.[23,28] More importantly, doping alters the energy band structure, improving alignment with perovskite and potentially reducing trap-state density.[23] For example, Yang et al. found that Y-doping SnO_2 slightly widens the band gap from 3.65 to 3.70 eV. After 3% yttrium doping, the CB minimum (CBM) of yttrium-doped SnO_2 (Y:SnO_2) is ≈ 0.13 eV higher than SnO_2.[29] Similarly, Song et al. observed that yttrium doping shifts the CBM of SnO_2 by 0.19 eV toward more positive values.[30] In both cases after yttrium doping, the CB of Y:SnO_2 is closer to the CB of the perovskite, enhancing energy band alignment and improving V_{OC}.

The potential of Y:SnO_2 as an alternative ETL to fullerenes and their derivatives in inverted PSCs is particularly noteworthy due to its low-temperature solution processibility and superior optoelectronic properties.[23] Additionally, SnO_2 is several orders of magnitude less expensive than C_{60} (Table S1). However, the broader application of solution-processed SnO_2 in inverted PSCs has been limited, mainly because of the solvent incompatibility between the SnO_2 dispersion medium and the perovskite absorber layer. In our prior research, we have successfully demonstrated the viability of using solution-processible, ligand-stabilized SnO_2 nanoparticles as an ETL in an inverted PSC architecture with $MAPbI_3$ and $MA_{0.6}FA_{0.4}Pb(I_{0.95}Br_{0.05})_3$.[31–33] From those studies, it was found that devices with 2 mol % Y:SnO_2 have enhanced performance compared to devices with pristine SnO_2.[32]

To demonstrate the broad utility of the Y:SnO_2 nanoparticles for use in multiple architectures, including single-junction and tandem devices, the current study reports their application with a wide array of perovskite compositions commonly employed in literature. To provide a guide for the use of the Y:SnO_2 particles on other surfaces, we also provide a rationale for particle stability based on Hansen solubility parameters allowing for customized solvent choices in future applications. The results demonstrate the compatibility of this approach with four different lead halide perovskite layers: (1) $MAPbI_3$ (MAPI), (2) $MA_{0.6}FA_{0.4}Pb(I_{0.95}Br_{0.05})_3$ (mixed cation, MC), (3) $Cs_{0.2}FA_{0.8}PbI_3$ (MA-free), and (4) $Cs_{0.1}(FA_{0.83}MA_{0.17})_{0.9}Pb(I_{0.85}Br_{0.15})_3$ (triple cation, TC) were studied. MAPI has been a popular choice due to its early adoption in PSC development. However, its energy band gap (E_g) of 1.57 eV exceeds the ideal 1.4 eV according to the Shockley–Queisser limit, which limits its performance.[34,35] $FAPbI_3$, with a band gap closer to the ideal at 1.47 eV, offers potentially better performance and greater thermal stability than MAPI. However, achieving photoactive phase stability in pure $FAPbI_3$ remains a challenge.[34,36] In MC perovskites, the partial replacement of MA present at the A-site with FA has improved thermal stability and performance compared to $MAPbI_3$.[37] Furthermore, the incorporation of the inorganic cation Cs in MA-free perovskites, specifically (Cs/FA)PbI_3, has been proposed to increase thermal and moisture stability.[38] TC mixed halide perovskites are another popular choice due to their improved efficiency and stability. In these perovskites, the simultaneous substitution of both A-site cations and X-site anions has shown superior thermal and moisture stability, further enhancing overall solar cell performance.[39] Furthermore, substituting iodide with bromide expands the band gap, making it suitable as a top cell in tandem devices.

A stable dispersion of pre-synthesized Y:SnO_2 nanoparticles was accomplished by functionalization with acetate ligands. The Y:SnO_2-A nanoparticle dispersions were then directly deposited via blade coating onto four different lead halide perovskite layers and a series of inverted flexible PSCs (f-PSC) on ITO-coated PET substrate were fabricated. The performance of these f-PSCs achieved champion power conversion efficiencies (PCEs) of 16.90%, 18.68%, 17.71%, and 20.41%, and average PCEs of 15.27%, 16.63%, 16.13%, and 19.02% for MAPI, MC, TC, and MA-free devices, respectively. The unencapsulated TC devices retained 90% of their initial average PCE after 600 h under continuous light illumination in an atmosphere-controlled box at 10% humidity and a temperature of 35 ± 5°C.

RESULTS AND DISCUSSION

Establishing solvent scope of SnO_2 dispersions

The synthesis of the Y:SnO_2 nanoparticles and the acetate functionalization were performed as described in detail in our previous work.[32] Figure S1 provides an overview of the ink preparation and subsequent blade coating processes. The basic scheme involves a precipitation reaction of a tin salt by adding a base. *In situ* doping with yttrium was achieved by adding a calculated amount of yttrium salt to the SnO_2 precursor during synthesis. The previously optimized yttrium concentration in SnO_2 of 2.0 mol % was used in the current study. The precipitate, once removed from the solution by centrifugation, was washed and dried, yielding a Y:SnO_2 as a powder, which was then refluxed with acetic acid to produce a concentrate of Y:SnO_2-A, the acetate-functionalized derivative of Y:SnO_2. The Y:SnO_2-A concentrate was estimated to have 40% w/v of Y:SnO_2 based on thermogravimetric analysis. The concentrated Y:SnO_2-A was diluted to the desired concentration of 1.6% w/v of Y:SnO_2 for direct deposition on the perovskite via the blade coating technique. Using an air knife with low air pressure (2–3 psi) during SnO_2-A deposition was found to be beneficial to promptly remove the bulk of the ethanol. This was followed by a short annealing period to remove any remaining residual solvent, which was optimized as 2 min at 100°C (Figure S6).

Table 1. Stability of Y:SnO_2-A dispersions in different solvents

Solvent type	Solvent	Stability[a]
Non-polar	Toluene	unstable
	Chlorobenzene	unstable
	Benzene	unstable
	Hexane	unstable
Aprotic polar	Acetone	unstable
	Acetonitrile	unstable
	Dimethylformamide (DMF)	unstable
	Tetrahydrofuran (THF)	unstable
	Methyl ethyl ketone (MEK)	unstable
	Gamma-butyrolactone (GBL)	stable
	Dimethyl sulfoxide (DMSO)	stable
	Diethyl ether	unstable
Protic polar	2 methoxy ethanol (2-ME)	stable
	Methanol	stable
	Ethanol	stable
	Propanol	stable
	2-Propanol (isopropanol)	stable
	1-Butanol	stable
	2-Butanol	unstable
	t-Butanol	unstable
	Isopentyl alcohol	unstable

[a]Inks were visually monitored for up to 6 hours and graded as stable (no visible changes) or unstable (precipitation or gelling).

The previous work demonstrated that Y:SnO_2-A yields stable dispersions in anhydrous ethanol. Ethanol, a polar solvent, is ideal for maintaining a stable dispersion of the metal oxide and is also volatile, allowing for minimized exposure to the perovskite layer. Inks for the direct deposition of HTLs or ETLs onto the perovskite thin films are limited by the perovskite compatibility of the solvent. However, it would be advantageous for scalable manufacturing to expand the selection of compatible solvents. The deposition of C_{60} directly onto a perovskite layer using blade coating has been achieved with non-polar solvents like chlorobenzene,[40] but such lower polarity solvents may affect the stability of metal oxide inks. Polar aprotic solvents are more suitable for metal oxides, but these are typically less volatile than alcohols and may require more energy to remove, potentially damaging the perovskite film. Thus, there is a balance between ink stability and evaporation, impacting the economics of high-volume manufacturing and perovskite compatibility and affecting device performance. This work considers the impact of the solvent on Y:SnO_2-A ink stability and perovskite compatibility.

The Y:SnO_2-A concentrate was diluted to 1.6% w/v of Y:SnO_2 in various solvents, categorized into three groups: non-polar, polar aprotic, and protic. The inks were visually monitored for up to 6 h and graded as stable dispersions (no visible changes) or unstable inks (precipitation or gelling) as summarized in Table 1. The Y:SnO_2-A dispersions have limited stability in most perovskite-compatible solvents with lower alcohols being the notable exceptions. Analysis of the Hansen parameters (δ_d = dispersion interaction, δ_p = polar interaction, δ_h = hydrogen-bond interaction)[41] shows that solvents with high hydrogen bonding and polar components were able to stabilize the Y:SnO_2-A (Figure S13). This is attributed to hydrogen bonding interactions with the surface-bound acetate and hydroxide groups on the Y:SnO_2-A particles. Meanwhile, longer chain alcohols with weaker hydrogen bonding interactions are unable to effectively prevent interparticle interactions resulting in precipitation. Alcohols that stayed above δ_h = 15 were also found to be stable. The most stable suspensions tested were made with ethanol and methanol. Interestingly, water has the highest hydrogen bonding component (δ_h = 42.3), but it immediately induces a gelling precipitation when added. The resulting matrix is a semi-solid, indicating an upper limit to the strength of the hydrogen bonding donation. Precipitation in low-hydrogen-bonding alcohols varied with the strength of the δ_h character. Alcohols between δ_h = 15 and 14 resulted in particle ripening indicated by an increase in haze followed by a bi-phasal separation. The bi-phasal separation could be remixed temporarily by stirring. Alcohols or solvents with δ_h < 14 induced immediate precipitation and could not be resuspended by stirring. Digital images of Y:SnO_2-A dispersions in the lower alcohols methanol, ethanol, propanol, 2-propanol (isopropanol), and butanol are presented in Figure S2. In all instances, the dispersions displayed good stability with the exception of isopropanol, which became cloudy within 1 h.

The perovskite compatibilities of the stable lower alcohol Y:SnO_2-A dispersions were evaluated by blade-coating them directly onto $MAPbI_3$ perovskite, simulating Y:SnO_2-A coating conditions. Evaluation of the X-ray diffraction (XRD) patterns (Figure S3) shows that the perovskite peak at 14.2° remained unchanged for all alcohol dispersions except for methanol, in which case a small peak at 12.7° associated

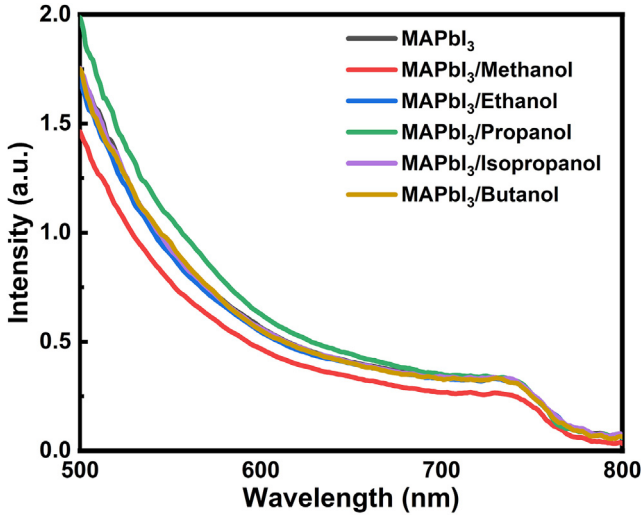

Figure 1. UV-vis absorption spectra of $MAPbI_3$ film after blade coating of methanol, ethanol, propanol, 2-propanol, and butanol directly onto $MAPbI_3$
During deposition, an air knife with a low air pressure of 3 psi was applied to remove the alcohol promptly, followed by 2 min of annealing at 100°C. The MAPbI3/methanol sample shows a reduction in the UV-vis absorption onset of MAPbI3 around 790 nm.

with lead iodide was observed. The UV-visible (UV-vis) spectra (Figure 1) of the perovskite coated with ethanol to butanol dispersions exhibited remarkable similarity to the control ($MAPbI_3$), indicating perovskite stability. However, methanol adversely affects the perovskite as evidenced by a reduced UV-Vis absorption onset of $MAPbI_3$ around 790 nm. The results clearly show that Y:SnO_2-A can be dispersed into several lower alcohols yielding an expanded library of available solvents for the deposition of Y:SnO_2 directly on perovskite. Additionally, the stability of the Y:SnO_2-A dispersions in the aprotic polar solvents gamma-butyrolactone (GBL) and DMSO suggests that solvent combinations could also be employed to improve ink stability and deposition. For the remainder of this work, anhydrous ethanol was used due to its good ink stability and faster evaporation rate.

Establishing compatibility of SnO_2 dispersions with diverse perovskites

Four different lead halide perovskite compositions (MAPI, MC, TC, and MA-free) covering a range of perovskite formulation, as described in the introduction, were investigated for their compatibility with Y:SnO_2-A dispersions. MAPI serves as a control since it is a standard, easy to fabricate perovskite. The MC (MC, TC, and MA-free) and mixed halide (MC and TC) perovskite materials are of particular interest as they are well suited for fabricating efficient multijunction solar cells due to their highly tunable band gap.[42] To investigate the compatibility of the Y:SnO_2-A dispersion as an ETL in PSCs with varied perovskite compositions, Y:SnO_2-A dispersions in anhydrous ethanol were directly deposited onto MAPI, MC, TC, and MA-free perovskite surfaces using blade coating. The ink formulation and blade coating parameters for MAPI and MC perovskites were derived from previously published work.[32,33] However, TC and MA-free inks required some optimization for blade coating under ambient conditions on the flexible PET-based substrate as detailed in the supplemental information.

The integrity of the perovskite layers post SnO_2 deposition was assessed by XRD, UV-vis spectroscopy, and SEM. Previously published works demonstrate the compatibility of fully solution-processed Y:SnO_2-A as an ETL in inverted PSCs with MAPI and MC perovskites.[31–33] The XRD patterns of MAPI, MC, MA-free, and TC perovskites before and after the deposition of Y:SnO_2-A dispersions are presented in Figure 2. Notably, the XRD patterns of all four perovskites with different compositions displayed a distinct peak around 14.2°, which aligns with expectations for a perovskite. This pattern remained consistent even after Y:SnO_2-A deposition, suggesting that the integrity of the perovskite layer is preserved. Importantly, no additional peak was found at 12.7°, a marker typically indicative of moisture-assisted degradation leading to the formation of PbI_2. These consistent XRD patterns affirm that the Y:SnO_2-A dispersion in anhydrous ethanol can be directly applied to halide perovskites with diverse compositions without causing noticeable surface degradation.

The UV-vis spectra of MAPI, MC, MA-free, and TC perovskites before and after Y:SnO_2-A deposition, as shown in Figure 3, reveal remarkable consistency. This consistency in the UV-vis spectra before and after Y:SnO_2-A deposition confirms that there are no significant changes in the optical absorption of the perovskite film. It emphasizes the preservation of the band edge of the absorption spectra and attests to the stability and integrity of those perovskites.[43,44] Taken together, the XRD and UV-vis analyses confirm that the adopted methodology ensures the perovskite layer remains pristine, underscoring its reliability for practical applications with commonly used halide perovskites, in addition to its applicability for MAPI and MC perovskites reported in earlier works.

The top surface SEM images of the perovskite film before and after ethanol exposure and Y:SnO_2 deposition are presented in the supplemental information (Figure S11). No noticeable variations are observed after washing the perovskite with ethanol. Further, the deposition of Y:SnO_2-A on the fully converted perovskite results in a uniform layer without noticeable pinholes. The results are consistent with our previous study in which the cross-sectional SEM image of the p-i-n device on a glass substrate clearly shows each individual layer, with no visible

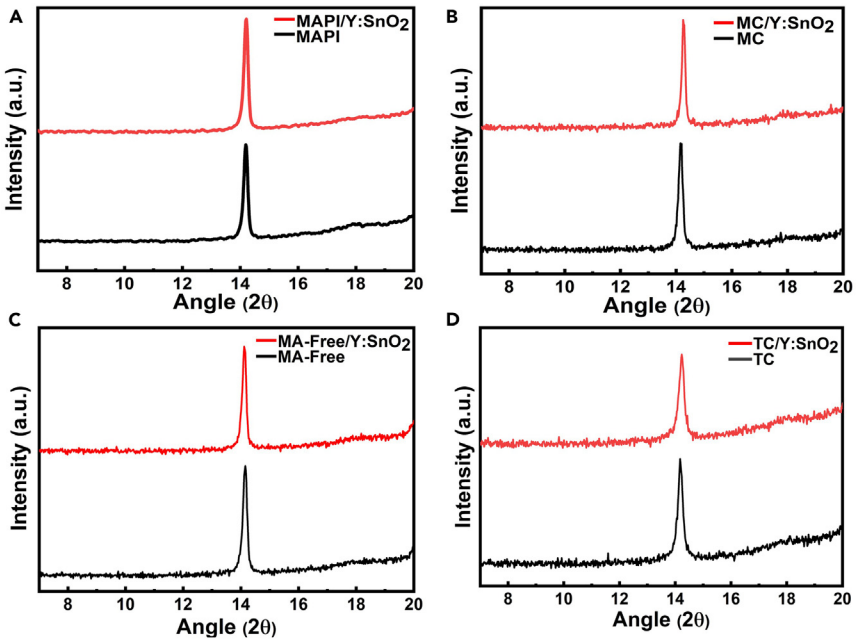

Figure 2. XRD patterns of perovskite films before and after the deposition of Y:SnO_2-A

XRD patterns before and after the deposition of a Y:SnO_2-A dispersion in ethanol via blade coating on (A) $MAPbI_3$ (MAPI), (B) $MA_{0.6}FA_{0.4}Pb(I_{0.95}Br_{0.05})_3$ (MC), (C) $Cs_{0.2}FA_{0.8}PbI_3$ (MA-free), and (D) $Cs_{0.1}(FA_{0.83}MA_{0.17})_{0.9}Pb(I_{0.85}Br_{0.15})_3$ (TC).

physical deformation of the perovskite layer due to the direct deposition of the SnO_2-A ink.[31] Additionally, the full-angle XRD patterns (Figure S12) show no signs of perovskite degradation or PbI_2 formation after Y:SnO_2 deposition.

We investigated photoluminescence quenching to assess the dynamics of electron transfer from a perovskite layer to a solution-phase-deposited Y:SnO_2 layer. Figure S4 presents the photoluminescence emission spectra of MAPI, MC, MA-free, and TC perovskite films interfaced with the solution-phase-deposited Y:SnO_2-A layer. Notably, the photoluminescence intensities of these perovskites are markedly quenched upon introducing the Y:SnO_2-A layer, implying a significant decrease in the charge carrier density within these perovskites. This reduction in carrier density aligns well with the theoretical expectation of efficient charge extraction by the solution-phase-deposited Y:SnO_2-A from the underlying perovskite layer.

The performance of a fully solution-processed Y:SnO_2-A thin film paired with various perovskite compositions such as MAPI, MC, MA-free, and TC was evaluated using an inverted device architecture (p-i-n). The overall device structures comprised: (1) PET/ITO/PTAA/PFN/MAPI/Y:SnO_2-A/BCP/Ag, (2) PET/ITO/PTAA/PFN/MC/Y:SnO_2-A/BCP/Ag, (3) PET/ITO/PTAA/PFN/MA-free/Y:SnO_2-A/BCP/Ag, and (4) PET/ITO/PTAA/PFN/TC/Y:SnO_2-A/BCP/Ag. In these configurations, polytriarylamine (PTAA) served as the HTL, and poly[(9,9-bis(3′-(N,N-dimethylamino)propyl)-2,7-fluorene)-alt-2,7-(9,9-dioctylfluorene)] (PFN) acted as an interfacial layer. A 3-nm-thick bathocuproine (BCP) buffer layer was deposited between Y:SnO_2 layer and Ag. This thin BCP buffer layer effectively reduces interfacial charge recombination between the SnO_2 ETL and Ag by maintaining proper ohmic contact.[31] PTAA, PFN, perovskite, and SnO_2 layers were deposited by one-step blade coating, whereas BCP and silver were deposited by thermal evaporation. We employed dry air knife quenching to promptly convert the perovskite precursor to an intermediate phase by eliminating excess solvent. Prior to the deposition of silver, any underlying layers were cleared away with GBL etching. Subsequently, a series of f-PSCs, each consisting of at least 10 pixels and having an active area of 0.1 cm^2, were fabricated.

The fabricated f-PSCs were measured under AM 1.5G simulated sunlight. Before measurement, the solar simulator was calibrated using an NREL-calibrated silicon reference photodiode with a KG5 filter to minimize the mismatch factor. The average and champion *J-V* performance statistics of f-PSCs utilizing MAPI, MC, MA-free, and TC perovskites are presented in Figure 4 and summarized in Table 2. The average V_{OC}, J_{SC}, fill factor (FF), and PCE values for devices employing TC perovskite as the photoactive layer are 1.15 ± 0.016 V, 22.91 ± 0.71 mA/cm^2, 72.17% ± 2.92%, and 19.02% ± 0.72%, respectively. For f-PSCs utilizing MAPI, MC, and MA-free perovskite as photoactive layers, the champion and average PCE are recorded as 16.9% and 15.27% ± 1.13%, 18.68% and 16.63% ± 1.18%, and 17.71% and 16.13% ± 0.87%, respectively. The champion *J-V* curves, a schematic of the device, and an image of the flexible device are presented in Figures 5A–5C. Notably, the highest-performing PSCs, featuring TC as the perovskite, demonstrated a PCE of 20.41%, accompanied by a remarkably high *Voc* of 1.17 V, *Jsc* of 23.56 mA/cm^2, and FF of 74.13%. However, there is a small *J-V* hysteresis between forward and reverse scan as shown in Figure S7 and Table S2. The improved performance of the TC PSCs is attributed to superior phase purity and enhanced moisture and thermal stability over MAPI, MC, and MA-free devices.[34,39,45]

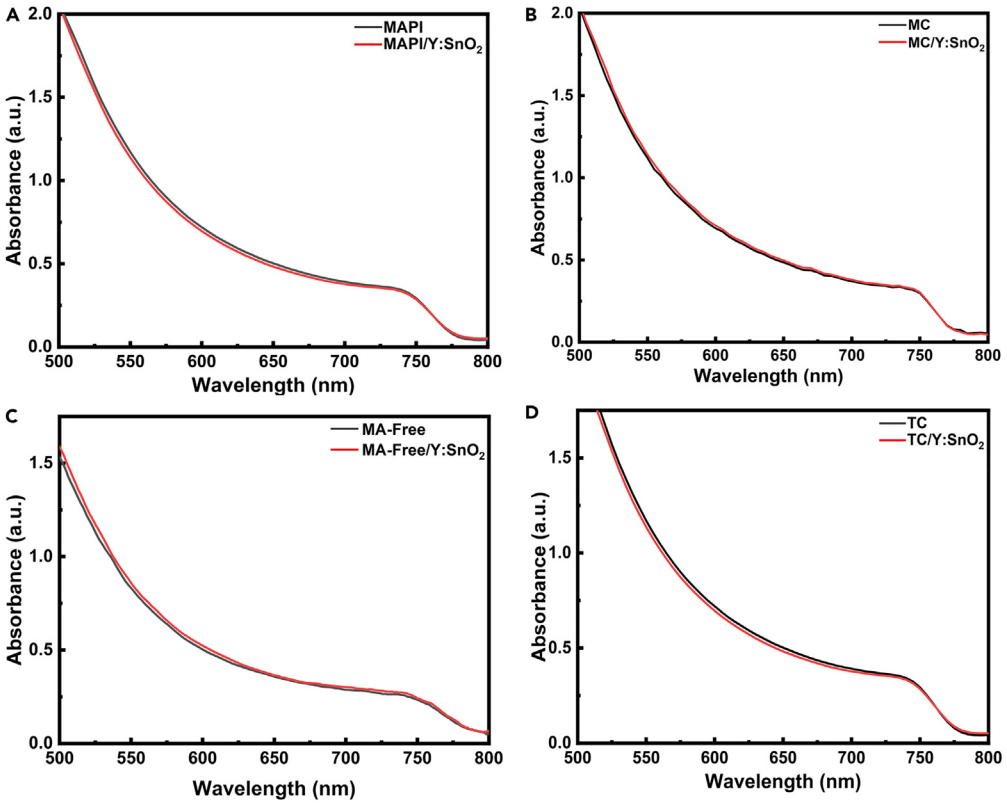

Figure 3. UV-vis spectra of perovskite films before and after the deposition of Y:SnO_2-A

UV-vis spectra before and after the deposition of a Y:SnO_2-A dispersion in ethanol via blade coating on (A) MAPbI3 (MAPI), (B) $MA_{0.6}FA_{0.4}Pb(I_{0.95}Br_{0.05})_3$ (MC), (C) $Cs_{0.2}FA_{0.8}PbI_3$ (MA-free), and (D) $Cs_{0.1}(FA_{0.83}MA_{0.17})_{0.9}Pb(I_{0.85}Br_{0.15})_3$ (TC).

To demonstrate larger area processing, up to 1 cm^2 TC PSCs were fabricated (Figure S8). The average PCE of thirteen 1 cm^2 devices was 13.40% ± 0.30%. Notably, the average J_{sc} and V_{oc} values of 22.85 ± 0.37 mA/cm^2 and 1.14 ± 0.02 V, respectively, are within experimental error of the 0.1 cm^2 devices. The decreased PCE of the larger area devices is due to a decreased FF associated with the low conductivity and high sheet resistance of the PET-ITO substrate, rated at 50 Ω/cm^2. This will increase the contact resistance which is evident from the angle of the *J-V* curve crossing the voltage axis, indicating a high series resistance of 4.74 Ω as calculated from the *J-V* curve of champion device. Dark current *J-V* characteristics and maximum power point tracking are provided in Figures S9 and S10. The operational stability of the f-PSC devices was evaluated under continuous light illumination inside a humidity-controlled box filled with nitrogen. Owing to the superior performance of the TC devices, they were chosen for stability testing. The unencapsulated devices maintained approximately 90% of their initial average PCE even after 600 h, as shown in Figure 5D.

Conclusions

In this work, we have explored the solvent compatibility of pre-synthesized Y:SnO_2 nanoparticles for direct deposition on four different lead halide perovskite layers, MAPI, MC, TC, and MA-free. Most notably, f-PSCs featuring TC perovskite as the photoactive layer achieved a peak efficiency of 20.41%, accompanied by a V_{OC} of 1.17 V, J_{SC} of 23.56 mA/cm^2, and FF of 74.13%. When employing MAPI, MC, and MA-free perovskites as the photoactive layers, the champion efficiencies reached 16.9%, 18.68%, and 17.71%, with average PCEs of 15.27% ± 1.13%, 16.63% ± 1.18%, and 16.13% ± 0.87%, respectively. These results are particularly noteworthy considering the fabrication method of blade coating on PET-ITO substrates.

The results expand our previous work with SnO_2 dispersions in anhydrous ethanol, demonstrating the compatibility of perovskite with several other lower alcohols. The use of co-solvent systems, combining lower alcohols with other protic and aprotic solvents, suggests a potential for a larger solvent space. This result broadens the solvent options for SnO_2-based ETL inks in p-i-n PSCs and opens possibilities for tandem devices that are dominated by C_{60}.

The compatibility of pre-synthesized Y:SnO_2 nanoparticles with MC (MC, TC, and MA-free) and mixed halide perovskites is particularly compelling due to their suitability for efficient multijunction solar cells, stemming from their highly tunable band gap ranging from 1.20 to 2.3 eV through compositional engineering.[42] It highlights the significance of the compatibility of fully solution-processed Y:SnO_2 ETLs with mixed halide compositions for cost-effective and stable Si/perovskite, perovskite/CIGS, and perovskite/perovskite tandem solar cells.

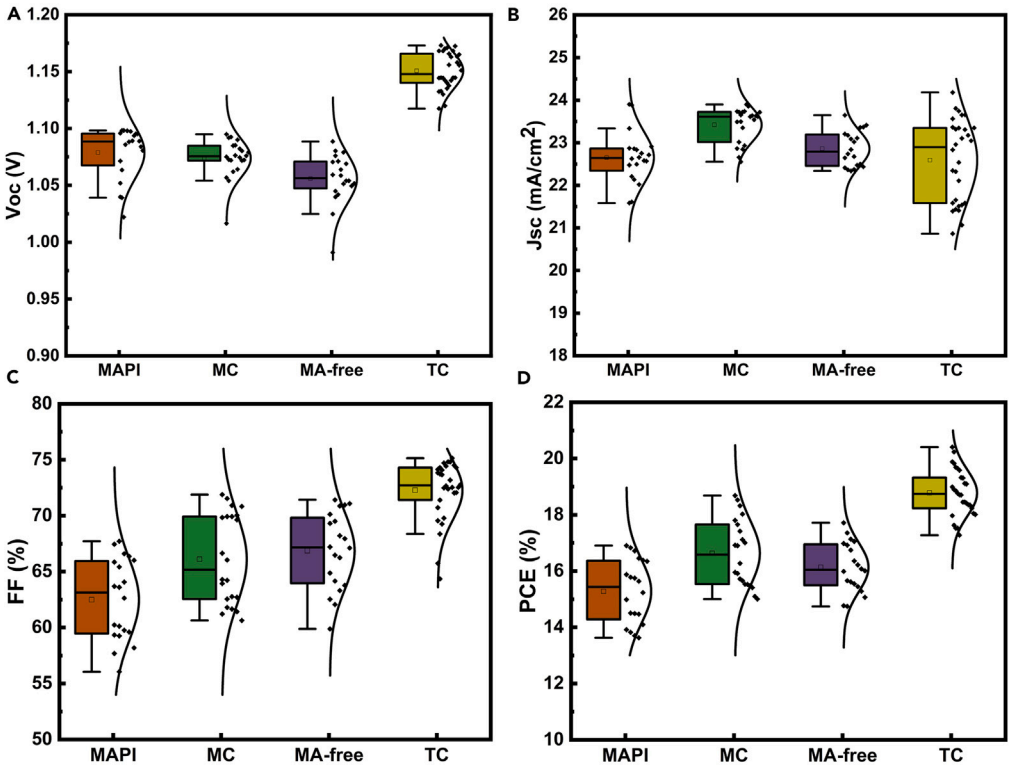

Figure 4. Comparison of device performance statistics for inverted f-PSCs with different perovskite absorbers

Boxplots of (A) open-circuit voltage (V_{OC}), (B) short-circuit current density (J_{SC}), (C) fill factor (FF), and (D) power conversion efficiency (PCE) for ITO-PET/PTAA/PFN/perovskite/Y:SnO_2-A/BCP/Ag devices with $MAPbI_3$ (MAPI), $MA_{0.6}FA_{0.4}Pb(I_{0.95}Br_{0.05})_3$ (MC), $Cs_{0.2}FA_{0.8}PbI_3$ (MA-free), or $Cs_{0.1}(FA_{0.83}MA_{0.17})_{0.9}Pb(I_{0.85}Br_{0.15})_3$ (TC) as the perovskite absorber.

Limitations of the study

This work addresses the deposition of SnO_2 (an ETL) directly on a perovskite layer in the preparation of flexible solar cell where the substrate is a polymer using scalable processes. The recent successes of perovskite/silicon tandems generally utilize an ETL deposited directly onto a perovskite film. The limitation of this study is the deposition processes required for the high-speed in-line production of perovskite/silicon tandems.

Table 2. Summary of the average photovoltaic performance statistics for inverted f-PSCs with different perovskite absorbers

Perovskite		V_{OC}[a] (V)	J_{SC}[a] (mA/cm^2)	FF[a] (%)	PCE[a] (%)
MAPI (0.1 cm^2)	average	1.078 ± 0.023	22.65 ± 0.60	62.48 ± 0.036	15.27 ± 1.13
	champion	1.096	22.87	67.45	16.90
MC (0.1 cm^2)	average	1.074 ± 0.017	23.42 ± 0.40	66.10 ± 0.040	16.63 ± 1.18
	champion	1.095	23.73	71.89	18.68
MA-free (0.1 cm^2)	average	1.056 ± 0.022	22.85 ± 0.42	66.8 ± 0.034	16.13 ± 0.87
	champion	1.088	23.21	70.13	17.71
TC (0.1 cm^2)	average	1.150 ± 0.016	22.91 ± 0.71	72.17 ± 2.92	19.02 ± 0.72
	champion	1.168	23.56	74.13	20.41
TC (1.0 cm^2)	average	1.14 ± 0.02	22.85 ± 0.37	51.55 ± 1.20	13.40 ± 0.30
	champion	1.16	23.59	50.95	13.95

V_{OC} is the open-circuit voltage, J_{SC} is the short-circuit current density, FF is the fill factor, and PCE is the power conversion efficiency.

[a]Device architecture is ITO-PET/PTAA/PFN/perovskite/Y:SnO_2-A/BCP/Ag where the perovskite is $MAPbI_3$ (MAPI), $MA_{0.6}FA_{0.4}Pb(I_{0.95}Br_{0.05})_3$ (MC), $Cs_{0.2}FA_{0.8}PbI_3$ (MA-free), or $Cs_{0.1}(FA_{0.83}MA_{0.17})_{0.9}Pb(I_{0.85}Br_{0.15})_3$ (TC).

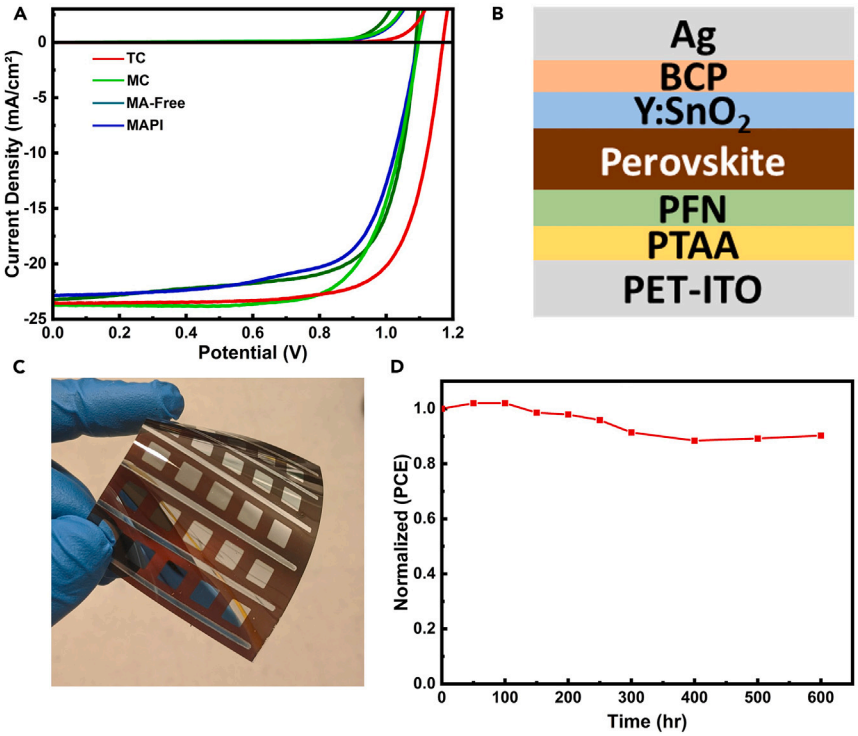

Figure 5. Champion device performance, architecture, and stability

(A) Champion light and dark *J-V* curves for ITO-PET/PTAA/PFN/perovskite/Y:SnO_2-A/BCP/Ag devices with perovskite = $MAPbI_3$ (MAPI), $MA_{0.6}FA_{0.4}Pb(I_{0.95}Br_{0.05})_3$ (MC), $Cs_{0.2}FA_{0.8}PbI_3$ (MA-free), or $Cs_{0.1}(FA_{0.83}MA_{0.17})_{0.9}Pb(I_{0.85}Br_{0.15})_3$ (TC), (B) schematic of device architecture, (C) photograph of flexible device, and (D) operational stability of ITO-PET/PTAA/PFN/perovskite/Y:SnO_2-A/BCP/Ag under continuous light illumination.

RESOURCE AVAILABILITY

Lead contact

Further information and requests for resources and reagents should be directed to and will be fulfilled by the lead contact, Craig A. Grapperhaus (craig.grapperhaus@louisville.edu).

Materials availability

This study did not generate new unique reagents.

Data and code availability

- Triple-cation device performance data, including reverse and forward scans, are presented in Table S2.
- This study does not report original new code
- Any additional information required to reanalyze the data reported in this paper is available from the lead contact upon request

ACKNOWLEDGMENTS

This work was funded in part or whole by the U.S. Department of Energy Solar Energy Technologies Office Award Number(s) DE-EE0008752.

AUTHOR CONTRIBUTIONS

Conceptualization, S.C., T.D., and C.A.G.; investigation, S.C., P.J.A., R.P., and N.A.; methodology, S.C., T.D., and C.A.G.; writing – original draft, S.C.; writing – review and editing, T.D. and C.A.G.; project administration, T.D. and C.A.G.

DECLARATION OF INTERESTS

The authors declare no competing interests.

STAR★METHODS

Detailed methods are provided in the online version of this paper and include the following:

- KEY RESOURCES TABLE

SUPPLEMENTAL INFORMATION

Supplemental information can be found online at https://doi.org/10.1016/j.isci.2024.110964.

Received: March 26, 2024
Revised: August 19, 2024
Accepted: September 11, 2024
Published: September 16, 2024

REFERENCES

1. Bai, S., Da, P., Li, C., Wang, Z., Yuan, Z., Fu, F., Kawecki, M., Liu, X., Sakai, N., Wang, J.T.-W., et al. (2019). Planar perovskite solar cells with long-term stability using ionic liquid additives. Nature *571*, 245–250. https://doi.org/10.1038/s41586-019-1357-2.
2. Jiang, Q., Zhao, Y., Zhang, X., Yang, X., Chen, Y., Chu, Z., Ye, Q., Li, X., Yin, Z., and You, J. (2019). Surface passivation of perovskite film for efficient solar cells. Nat. Photonics *13*, 460–466. https://doi.org/10.1038/s41566-019-0398-2.
3. Jiang, Q., Tong, J., Xian, Y., Kerner, R.A., Dunfield, S.P., Xiao, C., Scheidt, R.A., Kuciauskas, D., Wang, X., Hautzinger, M.P., et al. (2022). Surface reaction for efficient and stable inverted perovskite solar cells. Nature *611*, 278–283. https://doi.org/10.1038/s41586-022-05268-x.
4. NREL (2023). Best Research-Cell Efficiencies. https://www.nrel.gov/pv/assets/pdfs/best-research-cell-efficiencies.pdf.
5. Principe, J., Duarte, V.C., and Andrade, L. (2022). Inverted Perovskite Solar Cells: The Emergence of a Highly Stable and Efficient Architecture. Energy Technol. *10*, 2100952. https://doi.org/10.1002/ente.202100952.
6. Ji, T., Wang, Y.-K., Feng, L., Li, G.-H., Wang, W.-Y., Li, Z.-F., Hao, Y.-Y., and Cui, Y.-X. (2021). Charge transporting materials for perovskite solar cells. Rare Met. *40*, 2690–2711. https://doi.org/10.1007/s12598-021-01723-2.
7. Liu, S., Biju, V.P., Qi, Y., Chen, W., and Liu, Z. (2023). Recent progress in the development of high-efficiency inverted perovskite solar cells. NPG Asia Mater. *15*, 27. https://doi.org/10.1038/s41427-023-00474-z.
8. Shao, Y., Xiao, Z., Bi, C., Yuan, Y., and Huang, J. (2014). Origin and elimination of photocurrent hysteresis by fullerene passivation in $CH_3NH_3PbI_3$ planar heterojunction solar cells. Nat. Commun. *5*, 5784. https://doi.org/10.1038/ncomms6784.
9. Liang, Z., Zhang, Y., Xu, H., Chen, W., Liu, B., Zhang, J., Zhang, H., Wang, Z., Kang, D.-H., Zeng, J., et al. (2023). Homogenizing out-of-plane cations homogenise perovskite composition for solar cells. Nature *624*, 557–563. https://doi.org/10.1038/s41586-023-06784-0.
10. Liang, H., Yang, W., Xia, J., Gu, H., Meng, X., Yang, G., Fu, Y., Wang, B., Cai, H., Chen, Y., et al. (2023). Strain Effects on Flexible Perovskite Solar Cells. Adv. Sci. *10*, 2304733. https://doi.org/10.1002/advs.202304733.
11. Li, X., Yu, H., Liu, Z., Huang, J., Ma, X., Liu, Y., Sun, Q., Dai, L., Ahmad, S., Shen, Y., and Wang, M. (2023). Progress and challenges toward effective flexible perovskite solar cells. Nano-Micro Lett. *15*, 206. https://doi.org/10.1007/s40820-023-01165-8.
12. Bush, K.A., Palmstrom, A.F., Yu, Z.J., Boccard, M., Cheacharoen, R., Mailoa, J.P., McMeekin, D.P., Hoye, R.L.Z., Bailie, C.D., Leijtens, T., et al. (2017). 23.6%-efficient monolithic perovskite/silicon tandem solar cells with improved stability. Nat. Energy *2*, 17009. https://doi.org/10.1038/nenergy.2017.9.
13. Dong, S., Wan, Y., Wang, Y., Yang, Y., Wang, Y., Zhang, X., Cao, H., Qin, W., Yang, L., Yao, C., et al. (2016). Polyethylenimine as a dual functional additive for electron transporting layer in efficient solution processed planar heterojunction perovskite solar cells. RSC Adv. *6*, 57793–57798. https://doi.org/10.1039/C6RA09976A.
14. Chang, C.-Y., Huang, W.-K., Chang, Y.-C., Lee, K.-T., and Chen, C.-T. (2016). A solution-processed n-doped fullerene cathode interfacial layer for efficient and stable large-area perovskite solar cells. J. Mater. Chem. A *4*, 640–648. https://doi.org/10.1039/C5TA09080F.
15. Elnaggar, M., Elshobaki, M., Mumyatov, A., Luchkin, S.Y., Dremova, N.N., Stevenson, K.J., and Troshin, P.A. (2019). Molecular Engineering of the Fullerene-Based Electron Transport Layer Materials for Improving Ambient Stability of Perovskite Solar Cells. Sol. RRL *3*, 1900223. https://doi.org/10.1002/solr.201900223.
16. Cheacharoen, R., Rolston, N., Harwood, D., Bush, K.A., Dauskardt, R.H., and McGehee, M.D. (2018). Design and understanding of encapsulated perovskite solar cells to withstand temperature cycling. Energy Environ. Sci. *11*, 144–150. https://doi.org/10.1039/C7EE02564E.
17. Zahran, R., and Hawash, Z. (2022). Fullerene-Based Inverted Perovskite Solar Cell: A Key to Achieve Promising, Stable, and Efficient Photovoltaics. Adv. Mater. Interfac. *9*, 2201438. https://doi.org/10.1002/admi.202201438.
18. Anctil, A., Babbitt, C.W., Raffaelle, R.P., and Landi, B.J. (2011). Material and energy intensity of fullerene production. Environ. Sci. Technol. *45*, 2353–2359. https://doi.org/10.1021/es103860a.
19. Bai, Y., Yu, H., Zhu, Z., Jiang, K., Zhang, T., Zhao, N., Yang, S., and Yan, H. (2015). High performance inverted structure perovskite solar cells based on a PCBM: polystyrene blend electron transport layer. J. Mater. Chem. A *3*, 9098–9102. https://doi.org/10.1039/C4TA05309E.
20. Tian, C., Betancourt-Solis, G., Nan, Z., Liu, K., Lin, K., Lu, J., Xie, L., Echegoyen, L., and Wei, Z. (2021). Efficient and stable inverted perovskite solar cells enabled by inhibition of self-aggregation of fullerene electron-transporting compounds. Sci. Bull. *66*, 339–346. https://doi.org/10.1016/j.scib.2020.08.041.
21. Ai, M., Chen, M., and Yang, S. (2023). Recent Advances in Functionalized Fullerenes in Perovskite Solar Cells. Chin. J. Chem. *41*, 2337–2353. https://doi.org/10.1002/cjoc.202300105.
22. Park, S.Y., and Zhu, K. (2022). Advances in SnO2 for efficient and stable n–i–p perovskite solar cells. Adv. Mater. *34*, 2110438. https://doi.org/10.1002/adma.202110438.
23. Altinkaya, C., Aydin, E., Ugur, E., Isikgor, F.H., Subbiah, A.S., De Bastiani, M., Liu, J., Babayigit, A., Allen, T.G., Laquai, F., et al. (2021). Tin Oxide Electron-Selective Layers for Efficient, Stable, and Scalable Perovskite Solar Cells. Adv. Mater. *33*, 2005504. https://doi.org/10.1002/adma.202005504.
24. Lee, H.B., Jeon, M.-K., Kumar, N., Tyagi, B., and Kang, J.-W. (2019). Boosting the Efficiency of SnO2-Triple Cation Perovskite System Beyond 20% Using Nonhalogenated Antisolvent. Adv. Funct. Mater. *29*, 1903213. https://doi.org/10.1002/adfm.201903213.
25. Jiang, Q., Zhang, L., Wang, H., Yang, X., Meng, J., Liu, H., Yin, Z., Wu, J., Zhang, X., and You, J. (2016). Enhanced electron extraction using SnO2 for high-efficiency planar-structure HC(NH2)(2)PbI3-based perovskite solar cells. Nat. Energy *2*, 16177. https://doi.org/10.1038/nenergy.2016.177.
26. Steier, L., Tress, W., Saliba, M., Neutzner, S., Matsui, T., Giordano, F., Jacobsson, J., Kandada, A.S., and Zakeeruddin, S. (2015). Highly efficient planar perovskite solar cells through band alignment engineering. Energy Environ. Sci. *8*, 2928–2934. https://doi.org/10.1039/c5ee02608c.
27. Stolterfoht, M., Caprioglio, P., Wolff, C.M., Márquez, J.A., Nordmann, J., Zhang, S., Rothhardt, D., Hörmann, U., Amir, Y., Redinger, A., et al. (2019). The impact of energy alignment and interfacial recombination on the internal and external open-circuit voltage of perovskite solar cells. Energy Environ. Sci. *12*, 2778–2788. https://doi.org/10.1039/c9ee02020a.
28. Armstrong, P.J., Chapagain, S., Panta, R., Grapperhaus, C., and Druffel, T. (2023). Synthesizing and formulating metal oxide

nanoparticle inks for perovskite solar cells. Chem. Commun. *59*, 12248–12261. https://doi.org/10.1039/D3CC02830E.

29. Yang, G., Lei, H., Tao, H., Zheng, X., Ma, J., Liu, Q., Ke, W., Chen, Z., Xiong, L., Qin, P., et al. (2017). Reducing hysteresis and enhancing performance of perovskite solar cells using low-temperature processed Y-doped SnO_2 nanosheets as electron selective layers. Small *13*, 1601769. https://doi.org/10.1002/smll.201601769.
30. Song, J., Zhang, W., Wang, D., Deng, K., Wu, J., and Lan, Z. (2019). Colloidal synthesis of Y-doped SnO_2 nanocrystals for efficient and slight hysteresis planar perovskite solar cells. Sol. Energy *185*, 508–515. https://doi.org/10.1016/j.solener.2019.04.084.
31. Chapagain, S., Chandrasekhar, P.S., McGott, D., Bramante, R.C., van Hest, M.F.A.M., Reese, M.O., Druffel, T., and Grapperhaus, C.A. (2021). Direct Deposition of Nonaqueous SnO_2 Dispersion by Blade Coating on Perovskites for the Scalable Fabrication of p–i–n Perovskite Solar Cells. ACS Appl. Energy Mater. *4*, 10477–10483. https://doi.org/10.1021/acsaem.1c01287.
32. Chapagain, S., Martin, B., Armstrong, P., Perkins, C.L., Reese, M.O., Druffel, T., and Grapperhaus, C.A. (2023). High Performing Inverted Flexible Perovskite Solar Cells via Solution Phase Deposition of Yttrium-Doped SnO_2 Directly on Perovskite. ACS Appl. Energy Mater. *6*, 4496–4502. https://doi.org/10.1021/acsaem.2c03720.
33. Martin, B., Chapagain, S., Armstrong, P., Grapperhaus, C.A., Reese, M.O., and Druffel, T. (2023). IPL-Annealed Mixed-Cation Perovskites with Robust Coating Window toward Scalable Manufacturing of Commercial Perovskite Solar Cells. ACS Appl. Energy Mater. *6*, 5207–5216. https://doi.org/10.1021/acsaem.3c00134.
34. Jena, A.K., Kulkarni, A., and Miyasaka, T. (2019). Halide perovskite photovoltaics: background, status, and future prospects. Chem. Rev. *119*, 3036–3103. https://doi.org/10.1021/acs.chemrev.8b00539.
35. Cheng, H.-E., Tian, D.-C., and Huang, K.-C. (2012). Properties of SnO_2 films grown by atomic layer deposition. Procedia Eng. *36*, 510–515. https://doi.org/10.1016/j.proeng.2012.03.074.
36. Eperon, G.E., Stranks, S.D., Menelaou, C., Johnston, M.B., Herz, L.M., and Snaith, H.J. (2014). Formamidinium lead trihalide: a broadly tunable perovskite for efficient planar heterojunction solar cells. Energy Environ. Sci. *7*, 982–988. https://doi.org/10.1039/C3EE43822H.
37. Wang, C., Zhao, D., Yu, Y., Shrestha, N., Grice, C.R., Liao, W., Cimaroli, A.J., Chen, J., Ellingson, R.J., Zhao, X., and Yan, Y. (2017). Compositional and morphological engineering of mixed cation perovskite films for highly efficient planar and flexible solar cells with reduced hysteresis. Nano Energy *35*, 223–232. https://doi.org/10.1016/j.nanoen.2017.03.048.
38. Leijtens, T., Bush, K., Cheacharoen, R., Beal, R., Bowring, A., and McGehee, M.D. (2017). Towards enabling stable lead halide perovskite solar cells; interplay between structural, environmental, and thermal stability. J. Mater. Chem. A *5*, 11483–11500. https://doi.org/10.1039/C7TA00434F.
39. Saliba, M., Matsui, T., Seo, J.Y., Domanski, K., Correa-Baena, J.P., Nazeeruddin, M.K., Zakeeruddin, S.M., Tress, W., Abate, A., Hagfeldt, A., and Grätzel, M. (2016). Cesium-containing triple cation perovskite solar cells: improved stability, reproducibility and high efficiency. Energy Environ. Sci. *9*, 1989–1997. https://doi.org/10.1039/c5ee03874j.
40. Marques, A.S., Faria, R.M., Freitas, J.N., and Nogueira, A.F. (2021). Low-temperature blade-coated perovskite solar cells. Ind. Eng. Chem. Res. *60*, 7145–7154. https://doi.org/10.1021/acs.iecr.1c00789.
41. Hansen, C.M. (2000). Hansen Solubility Parameters - A Users Handbook (CRC Press LLC).
42. Nie, T., Fang, Z., Ren, X., Duan, Y., and Liu, S.F. (2023). Recent Advances in Wide-Bandgap Organic–Inorganic Halide Perovskite Solar Cells and Tandem Application. Nano-Micro Lett. *15*, 70. https://doi.org/10.1007/s40820-023-01040-6.
43. Kundu, S., and Kelly, T.L. (2020). In situ studies of the degradation mechanisms of perovskite solar cells. EcoMat *2*, e12025. https://doi.org/10.1002/eom2.12025.
44. Hwang, I., Jeong, I., Lee, J., Ko, M.J., and Yong, K. (2015). Enhancing stability of perovskite solar cells to moisture by the facile hydrophobic passivation. ACS Appl. Mater. Interfaces *7*, 17330–17336. https://doi.org/10.1021/acsami.5b04490.
45. Dong, C., Wang, Z.-K., and Liao, L.-S. (2020). Progress of triple cation organometal halide perovskite solar cells. Energ. Tech. *8*, 1900804. https://doi.org/10.1002/ente.201900804.
46. Ouyang, Z., Yang, M., Whitaker, J.B., Li, D., and van Hest, M.F.A.M. (2020). Toward Scalable Perovskite Solar Modules Using Blade Coating and Rapid Thermal Processing. ACS Appl. Energy Mater. *3*, 3714–3720. https://doi.org/10.1021/acsaem.0c00180.

STAR★METHODS

KEY RESOURCES TABLE

REAGENT or RESOURCE	SOURCE	IDENTIFIER
Chemicals, peptides, and recombinant proteins		
Toluene	Millipore Sigma	CAS: 108-88-3
Chlorobenzene	Millipore Sigma	CAS: 108-90-7
Benzene	Millipore Sigma	CAS: 71-43-2
Hexane	Millipore Sigma	CAS: 110-54-3
Acetone	Millipore Sigma	CAS: 67-64-1
Acetonitrile	Millipore Sigma	CAS: 75-05-8
Dimethylformamide (DMF)	Millipore Sigma	CAS: 68-12-2
Tetrahydrofuran (THF)	Millipore Sigma	CAS: 109-99-9
Methyl ethyl ketone (MEK)	Millipore Sigma	CAS: 78-93-3
Gamma-butyrolactone (GBL)	Millipore Sigma	CAS: 96-48-0
Dimethyl sulfoxide (DMSO)	Millipore Sigma	CAS: 67-68-5
Diethyl ether	Millipore Sigma	CAS: 60-29-7
2-Methoxy ethanol (2-ME)	Millipore Sigma	CAS: 109-86-4
Methanol	Millipore Sigma	CAS: 67-56-1
Ethanol	Millipore Sigma	CAS: 67-56-1
Propanol	Millipore Sigma	CAS: 71-23-8
2-Propanol (isopropanol)	Millipore Sigma	CAS: 67-63-0
1-Butanol	Millipore Sigma	CAS: 71-36-3
2-Butanol	Millipore Sigma	CAS: 78-92-2
t-Butanol	Millipore Sigma	CAS: 75-65-0
Isopentyl alcohol	Millipore Sigma	CAS: 123-51-3
N-Methyl-2-pyrrolidone (NMP)	Millipore Sigma	CAS: 872-50-4
Cesium iodide (CsI)	TCI	CAS: 7789-17-5
Methylammonium bromide (MABr)	Greatcell Solar	CAS: 6876-37-5
Lead(II) Bromide ($PbBr_2$)	TCI	CAS: 10031-22-8
Formamidinium iodide (FAI)	Greatcell Solar	CAS: 879643-71-7
Lead(II) Iodide (PbI_2)	TCI	CAS: 10101-63-0
Methylammonium chloride (MACl)	Greatcell Solar	CAS: 593-51-1
ITO coated polyethylene terephthalate (PET/ITO)	VDI Louisville	
Poly[bis(4-phenyl)(2,4,6-trimethylphenyl)amine (PTAA)	Millipore Sigma	CAS: 1333317-99-9
Poly [(9,9-bis(3′-(N,N-dimethylamino)propyl)-2,7-fluorene)-alt-2,7-(9,9–dioctylfluorene)] (PFN)	Millipore Sigma	CAS: 673474-74-3
Yttrium doped tin(IV) oxide – acetate (Y:SnO_2-A)	Prepared as previously reported[32]	
Bathocuproine (BCP)		CAS: 4733-39-5

METHOD DETAILS

Stability of the Y:SnO_2-A dispersions in different solvents

Dispersions of Y:SnO_2-A inks were prepared in different solvent to evaluate their stability. A Y:SnO_2-A concentrate was prepared as previously described.[32] A portion of the concentrate was added to the different solvents to obtain a final concentration of 1.6% w/v. Y:SnO_2-A concentrate was added dropwise to a continuously stirred solvent of interest during dilution. The samples were visually monitored for up to 6 h and graded as stable dispersions (no visible changes) or unstable inks (precipitation or gelling). Data is provided in Table 1. Overall, Y:SnO_2-A dispersions are unstable in the majority of the perovskite compatible solvents with the exception of lower alcohols and the higher boiling

point aprotic polar solvents GBL and DMSO. Digital images of the dispersions in the lower alcohols as three time points (initial, 1 h, 6 h) are provided in Figure S2. All dispersions in lower alcohols were stable for at least 6 h with the exception of isopropanol, which became cloudy within 1 h and precipitated within 6 h.

Preparation of perovskite precursor solutions

The MAPI perovskite precursor solution was prepared at a concentration of 1.2M using a solvent system composed of DMF, DMSO, and NMP in a volume ratio of 0.91:0.07:0.02.[46] Specifically, 0.159 g of MAI and 0.461 g of PbI_2 were measured and combined in a glass container. Then, 758 μL of DMF, 58 μL of DMSO, and 17 μL of NMP were added to the mixture. The solution was stirred continuously for several hours to ensure thorough mixing.

The triple cation perovskite precursor solution, $Cs_{0.1}(FA_{0.83}MA_{0.17})_{0.9}Pb(I_{0.85}Br_{0.15})_3$, with a concentration of 1.1 M, was prepared using a solvent system comprising DMF, THF, and NMP. For this, 0.312 g of CsI, 0.0206 g of MABr, 0.0654 g of $PbBr_2$, 0.154g of FAI, and 0.471 g of PbI_2 were measured and mixed in a glass container. Five mol % of MACl was added to the mixture to enhance the quality of the perovskite crystals. Subsequently, 880 μL of DMF, 150 μL of THF, and 70 μL of NMP were introduced into the mixture. The mixture was then left to stir overnight inside a glove box.

The MA-Free perovskite ($Cs_{0.2}FA_{0.8}PbI_3$) precursor solution with a concentration 1.1 M, was prepared using a solvent system of DMF and NMP. The components included 0.0623 g of CsI, 0.165 g of FAI, and 0.553 g of PbI_2 mixed in a container. To improve the crystal quality of the perovskite, Five mol % of MACl was added. Finally, 1030 μL of DMF and 70 μL of NMP were introduced into the mixture. The mixture was then left to stir overnight inside a glove box.

Device fabrication

Inverted PSCs were fabricated on a flexible PET/ITO substrate (50 Ω sheet resistance). A portion of ITO PET substrate was cut into 6 × 8 in. pieces, and they were blown with an air gun and wiped using IPA. Those cleaned PET substrates were treated with UV-Ozone for 15 min immediately before the sequential deposition of PTAA, PFN, Perovskite, and Y:SnO_2-A dispersion by blade coating inside a dry box. A PTAA solution was prepared by dissolving 8 mg of PTAA in 1 mL of toluene. A 35 μL of the PTAA solution was used for blade coating with a blade gap of 100 μm at a coating speed of 10 mm/s, then heating at 100°C for 10 min and cooling to room temperature. Next, 30 μL of a 0.4 mg/mL PFN solution in methanol was blade-coated on the PTAA layer at a coating speed of 10 mm/s with a blade gap of 100 μm. The triple cation and MA-Free perovskite precursor solutions were deposited by blade coating with a blade gap of 150 μm and at a coating speed of 10 mm/s. During the deposition of perovskite precursor solutions, the wet films were predried using a dry-air knife. Immediately after the air-knife drying, triple cation perovskite was annealed at 120°C for 10 min, and MA-Free perovskite was annealed at 130°C for 10. Figure S5A shows the annealing optimization of TC perovskite, which demonstrates that TC perovskite precursor was fully converted to the photoactive perovskite phase at a temperature of 120°C for 10 min without any intermediate phase. Figure S5B shows the blade-coated TC perovskite film before annealing but after air knife treatment and Figure S4C shows the TC film after annealing.

The optimal annealing temperature for MA-free perovskite differs TC perovskite. As shown in Figure S6A, the optimum annealing condition for MA-free perovskite is at 130°C for 10 min resulting in a fully converted perovskite film, Figure S6B. This condition is necessary for complete conversion to MA-free perovskite. However, it is noted that at annealing conditions of 120°C for 10 min, at 130°C for 5 min, and at 140°C for 5 min, NMP adducts are still present. This indicates that these conditions are either insufficient in temperature or duration for complete conversion, leading to the residual presence of adducts.

Finally, 30 μL of the Y-SnO_2-A dispersion in anhydrous ethanol was deposited onto the perovskites using a blade with a gap of 100 μm, and the coating was applied at a speed of 10 mm/s. This process was followed by annealing at 100°C for 2 to 3 min. The optimized thickness of the SnO_2 ETL was measured to be 36.7 ± 3.4 nm from the cross-sectional image of perovskite solar cells on the glass substrate.[31] When we increased the concentration of SnO_2 dispersion from 2% to 4%, the average series resistance value of the SnO_2 device has increased from 11.39 Ωcm^2 to 21.63 Ω cm^2. The *J*−*V* curve of the device having a thicker SnO_2 layer shows severe deviation due to very high series resistance.[31] During the deposition of Y:SnO_2-A, a low-air knife with a pressure of less than five psig was employed to remove the Ethanol rapidly. The fabrication of f-PSCs having device architectures (a) PET/ITO/PTAA/PFN/MAPI/Y:SnO_2-A/BCP/Ag, (b) PET/ITO/PTAA/PFN/MC/Y:SnO_2-A/BCP/Ag, (c) PET/ITO/PTAA/PFN/MA-free/Y:SnO_2-A/BCP/Ag and, (d) PET/ITO/PTAA/PFN/TC/Y:SnO_2-A/BCP/Ag and an active area of 0.1 cm^2 was completed by depositing 5nm of BCP and 100 nm of silver employing thermal evaporation. The fabricated f-PSCs were measured under AM 1.5G simulated sunlight. Before measurement, the solar simulator was calibrated using an NREL-calibrated silicon reference photodiode with a KG5 filter to minimize the mismatch factor. The fabricated f-PSCs were measured under AM 1.5G simulated sunlight in an ambient environment with humidity between 40 and 50%. Before measurement, the solar simulator was calibrated using an NREL-calibrated silicon reference photodiode with a KG5 filter to minimize the mismatch factor. The cells underwent light soaking for 5 min before the pixel measurements. The *J-V* curves were obtained using an Autolab PGSTAT128-N potentiostat and a height-adjustable superstrate simulator equipped with an AM 1.5G filter from a Newport LCS-100 lamp. The potential sweep was set to 100 mV/s for the *J-V* measurement. We conducted a stability study of unencapsulated TC PSCs within a humidity-controlled system. This study was carried out at a consistent humidity range of 10–15%. Simultaneously, the temperature of the system was maintained at 35 ± 5°C. We employed an array of LED lamps for illumination, with the light intensity calibrated to a range of 0.8–1 sun, using a reference photodiode.

QUANTIFICATION AND STATISTICAL ANALYSIS

In the manuscript, all *J-V* data presented are derived from the mean values of at least triplicate experimental readings. The statistical analysis and data processing were conducted utilizing OriginPro 2024b Learning Edition software. Data were expressed as mean ± SEM (standard error of mean).